AGU100 ADVANCING EARTH AND SPACE SCIENCE

Geophysical Research Letters

RESEARCH LETTER
10.1029/2018GL079142

Key Points:
- The spatial structure and temporal development of stratospheric inertial instability at 30-45 degrees north is characterized with GPS radio occultation measurements in December 2015
- The observed event is among the 0.1% strongest events in the ERA-Interim climatology; moderate events occur during 10% of the time
- Inertial instability events are a possible source of bias for gravity wave climatologies constructed from temperature measurements

Supporting Information:
- Supporting Information S1

Correspondence to:
M. Rapp,
markus.rapp@dlr.de

Citation:
Rapp, M., Dörnbrack, A., & Preusse, P. (2018). Large midlatitude stratospheric temperature variability caused by inertial instability: A potential source of bias for gravity wave climatologies. *Geophysical Research Letters*, *45*, 10,682–10,690. https://doi.org/10.1029/2018GL079142

Received 8 JUN 2018
Accepted 19 SEP 2018
Accepted article online 24 SEP 2018
Published online 4 OCT 2018

Large Midlatitude Stratospheric Temperature Variability Caused by Inertial Instability: A Potential Source of Bias for Gravity Wave Climatologies

M. Rapp[1,2], A. Dörnbrack[1], and P. Preusse[3]

[1]Deutsches Zentrum für Luft- und Raumfahrt, Institut für Physik der Atmosphäre, Oberpfaffenhofen, Germany, [2]Meteorologisches Institut München, Ludwig-Maximilians-Universität München, Munich, Germany, [3]Institute of Energy and Climate Research Forschungszentrum Jülich, Jülich, Germany

Abstract Stratospheric temperature perturbations (TP) that have previously been misinterpreted as due to gravity waves are revisited. The perturbations observed by radio occultations during December 2015 had peak-to-peak amplitudes of 10 K extending from the equator to midlatitudes. The vertically stacked and horizontally flat structures had a vertical wavelength of 12 km. The signs of the TP were 180° phase shifted between equatorial and midlatitudes at fixed altitude levels. High-resolution operational analyses reveal that these shallow temperature structures were caused by inertial instability due to the large meridional shear of the polar night jet at its equatorward flank in combination with Rossby wave breaking. Large stratospheric TP owing to inertial instability do frequently occur in the Northern Hemisphere (Southern Hemisphere) from October to April (April to October) in the 39 years of ECMWF Re-Analysis-Interim data. During 10% of the days, TP exceed 5 K (peak to peak).

Plain Language Summary The stratosphere is the part of the atmosphere between altitudes of ~15–50 km which contains the ozone layer that shields life from hazardous radiation. We use global stratospheric temperature measurements to learn about the variability of temperatures on vertical scales < 15 km. Usually, it is thought that such variations are caused by waves that are excited by the displacement of air when being lofted upward when, for example, the wind blows over mountains. The air then starts oscillating around its original height level because of gravity. Gravity waves are an important driver of stratospheric winds which, for example, determine the distribution of ozone. We present observations of large stratospheric temperature perturbations which could easily be misinterpreted as gravity waves. Combining the measurements with output of a numerical weather prediction model, we show that the observations are caused by a large-scale atmospheric instability called inertial instability. Using meteorological data spanning the past 40 years, we quantify when and how often such temperature perturbations of a certain size occur. Our results are important for properly constructing gravity wave climatologies (where inertial instability events must be excluded)—which are in turn an important input for the correct formulation of climate models.

1. Introduction

Inertial instability (II) is a hydrodynamic instability that occurs in rotating fluids and arises from an imbalance between the horizontal component of the pressure gradient force and the centrifugal force when the absolute value of angular momentum decreases with radius (Dunkerton, 1981). In the presence of II shallow zonal and meridional circulations arise in order to stabilize the flow by transporting angular momentum. Since mass continuity demands that meridional flows be accompanied by vertical motions (due to divergences and convergences) Dunkerton's theory also predicted the occurrence of stacked sheets of enhanced and reduced stratospheric temperatures. These patterns were first observed by Hitchman et al. (1987) with the Limb Infrared Monitor of the Stratosphere instrument on the Nimbus-7 satellite. Hitchman et al. (1987) called these temperature sheets *pancake structures* owing to their large aspect ratio of broad horizontal to narrow vertical extent (i.e., typical horizontal extent of hundreds to thousands of kilometers with a rather short vertical wavelength of 10–15 km) and negligible vertical tilt.

Since then, inertially unstable flows have been detected by independent limb-viewing satellite observations of stratospheric and mesospheric temperatures such as with the Cryogenic Limb Array Etalon Spectrometer on the Upper Atmosphere Research Satellite by Hayashi et al. (1998) and with the Cryogenic Infrared Spectrometer and Telescopes for the Atmosphere instrument on board the Shuttle Pallet Satellite by Smith and Riese (1999). Evidence for horizontal wind perturbations associated with inertially unstable circulations in the middle atmosphere was first presented by Fritts et al. (1992) using mesospheric wind observations with the Jicamarca radar and confirmed by Hayashi et al. (2002) who analyzed rocket sonde observations from the equatorial station Kwajalein. Finally, Sato and Dunkerton (2002) presented an analysis of a 4-year data set of high-resolution radiosondes over Japan and found horizontal velocity and temperature layers near the tropopause that they attributed to II.

Besides these very few direct observations, the excitation and properties of II have mainly been studied using numerical models and theory (e.g., Clark & Haynes, 1996; Griffiths, 2003; O'Sullivan & Hitchman, 1992; Rowe & Hitchman, 2015, 2016). A stratospheric II climatology based on analyses from the UK Met Office was presented by Knox and Harvey (2005), and the tropospheric II occurrence was documented using ECMWF Re-Analysis-Interim (ERA-Interim) data by Thompson et al. (2018). Importantly, both Knox and Harvey (2005) and Thompson et al. (2018) based their occurrence statistics of II on various instability criteria (see Thompson et al., 2018 for an in-depth discussion of the validity of various criteria) but they did not quantify the impact of the instability on stratospheric temperature variability.

Stratospheric temperature perturbations (TP) are commonly used to quantify gravity wave (GW) parameters like the gravity wave potential energy density and/or absolute values of the waves' momentum flux (e.g., Ehard et al., 2015; Ern et al., 2018; Geller et al., 2013). For this purpose, a suitable background profile is subtracted from the temperature profiles. Frequently, filtered profiles containing modes with vertical wavelengths λ_z >10–15 km are used to estimate the background temperature profile (e.g., Ehard et al., 2015; Preusse et al., 1999; Tsuda et al., 2000; Whiteway & Carswell, 1995). Nevertheless, filtering for modes with λ_z <15 km does not guarantee to exclude potential non-GW contributions: for example, tropical Kelvin waves or the stacked *pancake* structures produce similar vertical TP profiles as GWs for λ_z <15 km (see, e.g., Randel & Wu, 2005; Smith & Riese, 1999). Below, we show that large monthly mean gravity wave potential energy density values detected in stratospheric radio occultation (RO) data by Rapp et al. (2018) were erroneously attributed to GWs. Here we demonstrate that these TP were instead created by II. Since GW climatologies are generated to guide models for climate projection and weather prediction (Alexander et al., 2010), the occurrence rate of II must be known.

We present observations of the spatial and temporal structures of large stratospheric TP at λ_z <15 km in December 2015 as detected in GPS RO data. We use the European Centre for Medium-Range Weather Forecasts (ECMWF) operational analyses to investigate the source of these TP. Finally, we quantify the occurrence frequency of II-related stratospheric TP using ERA-Interim data from 1979 to 2016.

2. Data and Methods

We analyze temperature profiles derived from GPS RO measurements onboard the operational METOP-A and METOP-B satellites. Temperature profiles are available between 0- and 50-km altitude at an effective vertical resolution of 1–1.4 km, a precision of 0.1 K, and an accuracy of 1 K below 30 km and 1–10 K between 30 and 50 km (Kursinski et al., 1997; ROM SAF, 2014). Recently, Rapp et al. (2018) have systematically compared METOP RO temperatures to ECMWF operational analyses and found median temperature differences between −0.2 and +0.3 K below 30-km altitude, +1.0 K at 34-km altitude, and +2.2 K at 40-km altitude. Here we analyze RO temperatures from the period July 2015 to June 2016.

For the interpretation of RO observations we use ECMWF operational analyses for the investigation of a particular case and reanalysis data for the statistical evaluation of a long consistent data set. The 6-hourly operational analyses of ECMWF's Integrated Forecast System (IFS) for December 2015 have a horizontal resolution of about 16 km (T_L1279). One hundred thirty-seven vertical levels with a spacing between 0.5 km at 20-km altitude and 3.0 km at 70-km altitude are employed between the model top at a pressure level of 0.01 hPa (roughly 80-km altitude) and the surface (Malardel & Wedi, 2016). The second model data set is ERA-Interim, a global atmospheric reanalysis starting from 1979 which is based on a 2006 release of the IFS (Dee et al., 2011). The horizontal grid spacing of the data set is approximately 80 km (T_L255). For this study, model fields were

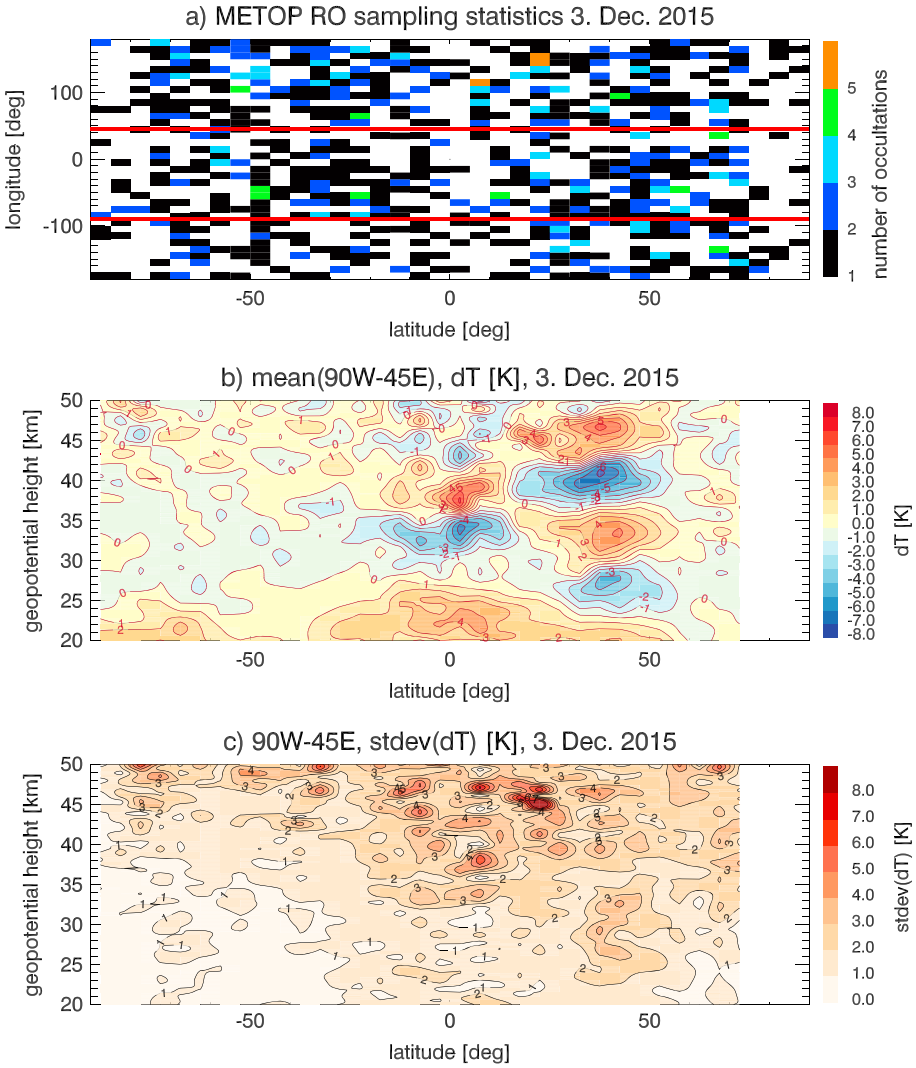

Figure 1. (a) Number of METOP-A and METOP-B radio occultations on 3 December 2015, on a latitude by longitude grid of 5° by 10°. Red horizontal lines mark longitudes between 90°W and 45°E. (b) Altitude versus latitude cross section of daily mean TP for the longitude range 90°W to 45°E and for the same day. (c) Standard deviations of TP shown in (b). TP = temperature perturbation; RO = radio occultation.

evaluated on 37 pressure levels between 1,000 and 1 hPa (corresponding to a vertical spacing of 2 km/4-km altitude at 20 km/40-km altitude).

Following Ehard et al. (2015) and Rapp et al. (2018), we determined TP from all data sets by applying a fifth-order Butterworth filter with a vertical cutoff wavelength of 15 km to separate temperature profiles into a *background* and perturbations.

3. Observations

The analysis presented here was motivated by the observed large monthly mean GPWED values in the stratospheric METOP RO data between 30°N and 45°N and between 90°W and 45°E in December 2015 as presented in Figure 6d in Rapp et al. (2018). The visualization of the daily mean TP along latitude-altitude cross sections reveals that the monthly mean maxima were dominated by two events that each lasted a few days during December 2015. Figure 1b shows the TP of the first event on 3 December, the day of the maximum observed perturbations (see below).

Figure 1a shows the sampling statistics of the RO data for this single day. The majority of the 5° latitude by 10° longitude bins contains 1–5 soundings per day. This sampling allows us to derive mean TP (Figure 1b),

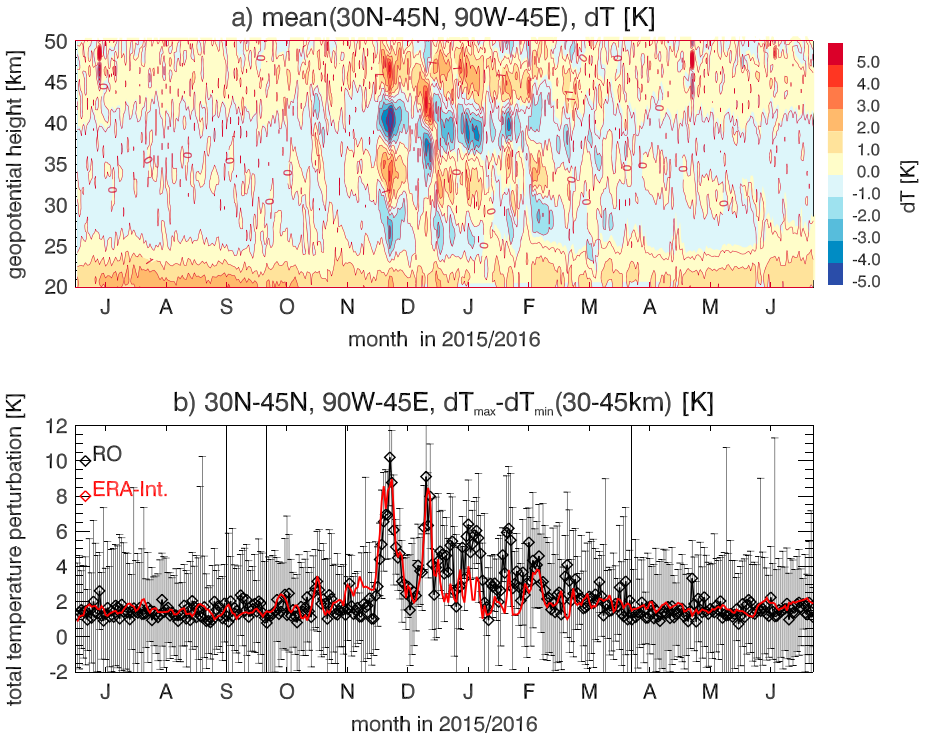

Figure 2. (a) Time series of daily mean TP versus altitude from METOP-A and METOP-B radio occultation data for the region 30–45°N and 90°W to 45°E for the period from 1 July 2015 to 30 June 2016. Tick marks on the *x* axis indicate the 15th of each month. (b) Time series of total temperature perturbation (maximum-minimum perturbation) between 30- and 45-km altitude in the time series shown in panel (a), in black, along with corresponding error bars. The red line indicates corresponding total TP from ERA-Interim for the same location and time. RO = radio occultation; ERA-Interim = ECMWF Re-Analysis-Interim.

and corresponding standard deviations (Figure 1c) in the longitude range between 90°W and 45°E based on 3–18 profiles (with a median of 8) per 5° latitude bin. The resulting cross sections of mean TP reveal vertically stacked bands of positive and negative values at 0–10°N and between 30°N and 45°N with amplitudes of 5–6 K (10–12 K peak to peak). The vertical wavelength of these patterns is ~12 km with a somewhat smaller value at the equator than at midlatitudes. Importantly, the TP at a fixed altitude are 180° phase shifted between equatorial and midlatitudes. The banded structures are basically *flat* and are thus reminiscent of *pancakes* as noted in the few earlier observations of II features. Note that we analyzed RO temperature structures at higher altitudes than is commonly done when RO data are used to determine GW properties. For this purpose, authors frequently show and analyze RO data below 35-km altitude (e.g., Schmidt et al., 2016) because of their well-known increasing random error with height (Marquardt & Healy, 2005). Here we do not identify GW signatures in single profiles but analyze planetary scale structures that emerge from the averaging of several profiles. The standard deviations shown in Figure 1c reveal that the observed TP are indeed real and significant, that is, larger than their standard deviations at the same height, except for latitudes north of ~ 70° where too few RO profiles (<3) were obtained.

Next, we turn to the temporal development of the midlatitude TP. Figure 2a shows daily mean TP versus time from 1 July 2015 to 30 June 2016, averaged over the region 30–45°N and 90°W to 45°E. This is the region where large stratospheric TP for the same day were found by Rapp et al. (2018). Moreover, midlatitude stratospheric II shows a maximum occurrence rate in this region (Knox & Harvey, 2005). Binning the profiles in this way results in 22–84 (median of 41) RO profiles per day. Inspection of their temporal evolutions reveals that the example shown in Figure 1 was the first in a sequence of several events during December 2015 and January 2016. The events each lasted up to 10 days with the two most prominent ones peaking on 3 December 2015 and 23 December 2015. The latter revealed similar pancake structures as in Figure 1. Figure 2b further shows the total TP $\Delta T_{total} = dT_{max} - dT_{min}$ in the altitude range 30–45 km as a function of time serving as a single quantitative measure of the events' strength. Error bars indicate the uncertainty of total TP, $\delta\Delta T_{total}$, owing to

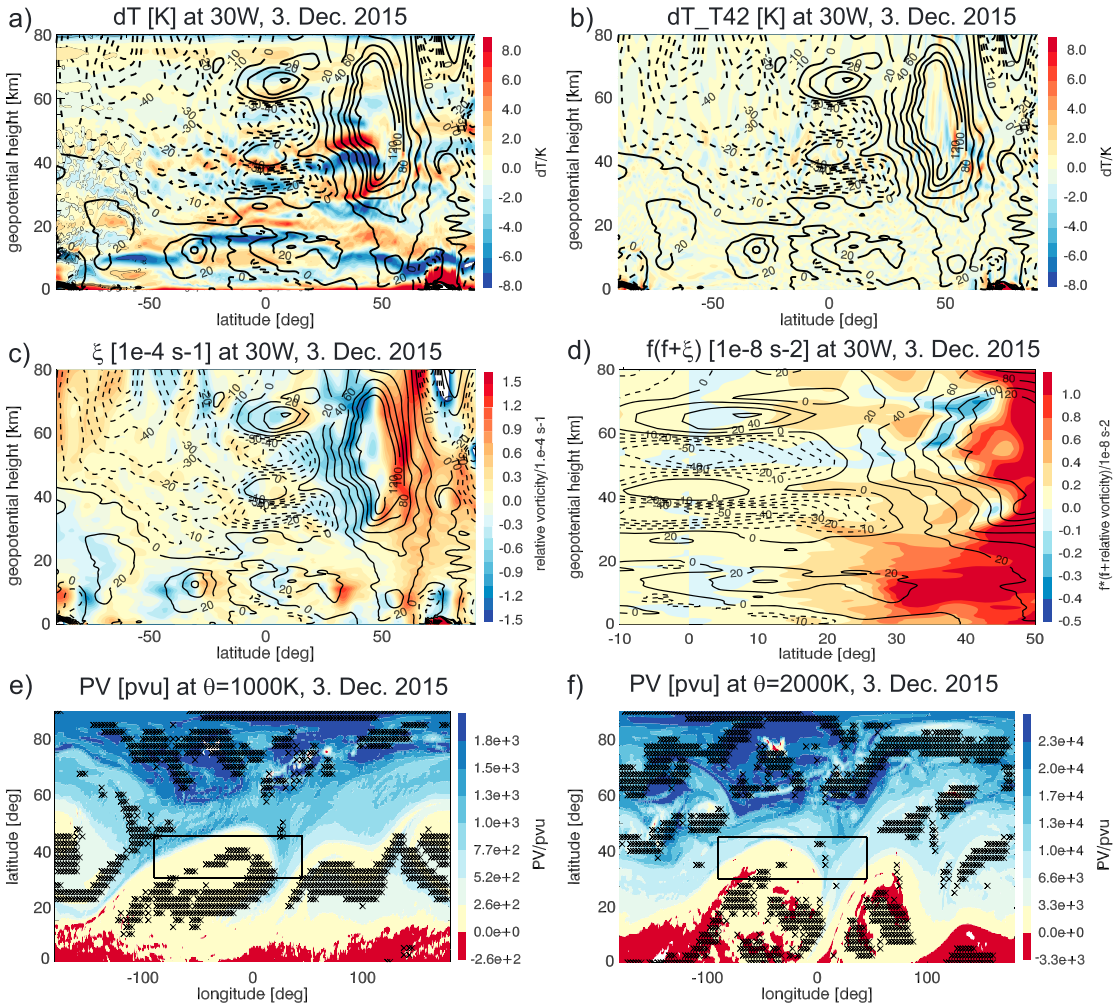

Figure 3. (a) Altitude-latitude cross section of TP (K; colors) determined by applying a fifth-order Butterworth filter with cutoff wavelength of 15 km to vertical temperature profiles at a longitude of 30°W based on ECMWF operational analyses for 3 December 2015, at 12 UT. The overplotted black lines are contours of the zonal wind in meter per second. (b) Same as (a) but for $dT_{T42} = T(T_L1279) - T(T_L42)$; see text for details. (c) Same as (a) but for relative vorticity ξ. (d) Same as (a) but for $f(f + \xi)$ and for a limited latitude range. (e) Latitude versus longitude cross section of potential vorticity (PV) at a level of fixed potential temperature of $\theta = 1000$ K ($\sim 34 \pm 2$-km altitude). Black crosses indicate regions of Rossby wave breaking diagnosed as $dPV/dy < 0$. Negative PV values (in red) are indicative of II (see text). The black rectangle marks the region where large midlatitude *pancake* structures were observed. (f) Same as (e) but for $\theta = 2000$ K ($\sim 48 \pm 3$-km altitude). TP = temperature perturbation; ECMWF = European Centre for Medium-Range Weather Forecasts; II = Inertial instability.

the standard deviation σ of dT_{max} and dT_{min} using error propagation. In the same panel, we have overplotted the total TP derived from ERA-Interim data for the same longitude-latitude region and time. The excellent agreement between ERA-Interim and RO data encourages us to use ECMWF model data to analyze the events in more detail and to compare the events observed in December 2015 to a climatology based on ERA-Interim.

4. Discussion

4.1. Detailed Analysis of the Event on 3 December 2015

We consider high-resolution ECMWF operational analysis data for 3 December 2015, at 12 UT. Figure 3a displays TP versus latitude and height at 30°W, that is, in the middle of the longitude region with large amplitudes. The ECMWF data clearly reproduce the large-amplitude pancake structures that we already identified in the RO observations. Note that the large perturbations seen below ~20 km are caused by the tropopause and the tropopause inversion layer as discussed in Rapp et al. (2018). Also, the ECMWF data clearly reproduce the observed 180° phase shift between TP at fixed altitudes around the equator and at midlatitudes. Importantly, the large midlatitude TP coincide with the very large meridional gradient of the zonal wind at the edge of the

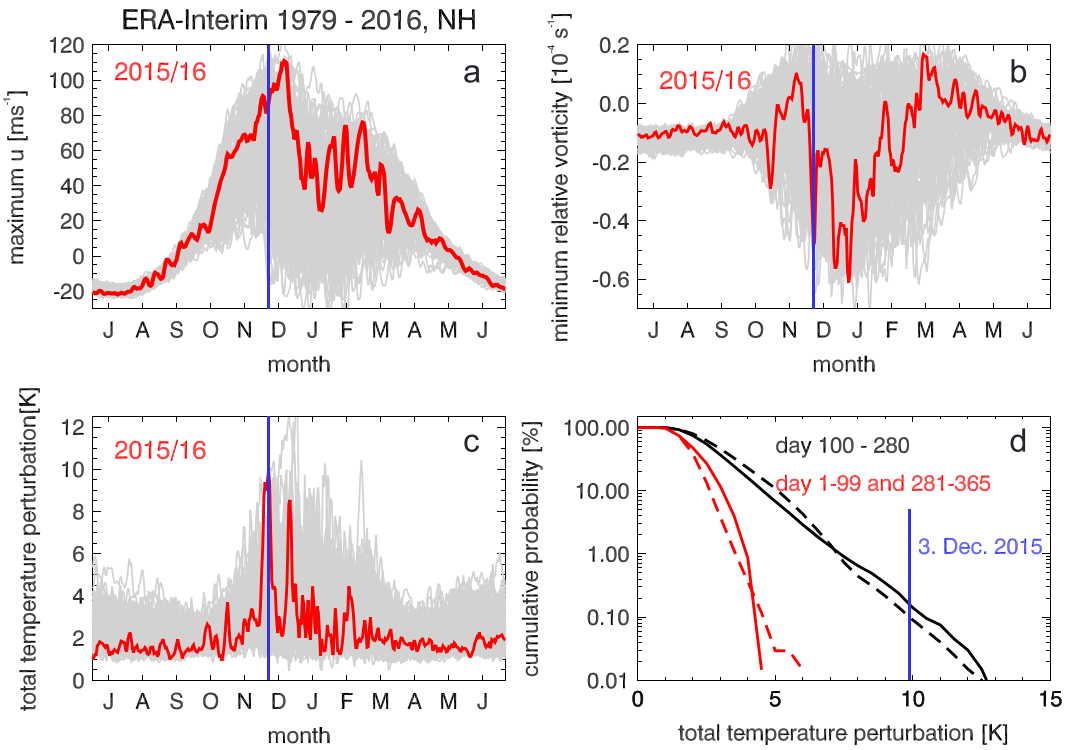

Figure 4. (a) Time series of daily mean values of maximum zonal wind in the latitude-longitude-altitude range of 30–45°N, 30- to 45-km altitude, and the longitude segments 90°W to 30°E, 30–150°E, 150°E to 90°W, for all years covered by ERA-Interim from 1979 to 2016. All time series start on 1 July in year 1 and end on 30 June in year 2. Tick marks on the *x* axis indicate the 15th of each month. (b) Time series of corresponding minimum mean relative vorticities. (c) Corresponding time series of total temperature perturbations. In panels (a)–(c), the time series 2015/2016 and 90°W to 30°E is plotted in red. (d) Cumulative probabilities of total TP for all years covered by ERA-Interim from 1979 to 2016. The red line indicates cumulative probabilities outside the season with large ΔT_{total} (days 1–99 and 281–365), whereas the black line indicates probabilities during the instability season (days 100–280, i.e., mid-October to mid-April). Dashed lines show corresponding cumulative probabilities for 30–45°S but shifted in time by 6 months. In each panel, the blue vertical line marks 3 December (or the corresponding ΔT_{total} value for the year 2015 in (d)). ERA-Interim = ECMWF Re-Analysis-Interim; TP = temperature perturbation; NH = Northern Hemisphere.

polar night jet (PNJ). The PNJ in December 2015 has been the strongest over the preceding 68 years (Matthias et al., 2016).

In contrast to the preceding analysis, Figure 3b shows TP derived by defining the background by synoptic-scale modes. For this purpose, we subtract IFS temperatures at the same spatial resolution but spectrally reduced to T_L42 from the T_L1279 fields. The resulting small perturbations in the range of ±1 K represent all subsynoptic motion scales, for example, due to GWs. Larger amplitudes of up to 3 K at the northward flank of the PNJ are likely due to mountain waves excited by flow over Greenland. Most importantly, however, the pancake structures are gone—underlining that they are not related to mesoscale GWs.

Furthermore, we analyze the standard criterion for II

$$f(f+\xi) < 0 \tag{1}$$

where f is the Coriolis parameter and $\xi = \partial v/\partial x - \partial u/\partial y$ is the relative vorticity where u and v are the zonal and meridional wind components, x is the west-to-east coordinate, and y is the south-to-north coordinate (e.g., Knox & Harvey, 2005; Thompson et al., 2018). Criterion 1 implies that a strong polar vortex with large $\partial u/\partial y$ at its equatorward flank should favor II. Indeed, the latitude-altitude cross section of ξ in Figure 3c depicts large negative values at the southern edge of the PNJ, that is, where large TP are observed. In order to identify the location of the II, what really matters is the minimum of $f(f+\xi)$ (Griffiths, 2008). Hence, we also delineate the quantity $f(f+\xi)$ in Figure 3d. This plot shows negative values of $f(f+\xi)$ at the equatorward edge of the PNJ at 30- to 40-km and 60- to 75-km altitude where also the global minimum of $f(f+\xi)$ is located. In addition,

criterion 1 is fulfilled close to the equator and in a broad latitude band from 0°N to 35°N at 50- to 60-km altitude. Criterion 1 for II is thus fulfilled for the event observed on 3 December 2015.

Note, however, that beyond criterion 1 also Rossby wave breaking has been related to the occurrence of II (e.g., Hayashi et al., 1998). According to O'Sullivan and Hitchman (1992) Rossby wave breaking may be diagnosed by

$$\partial PV/\partial y < 0 \tag{2}$$

on an isentropic level (θ = const.). Assuming stable stratification relation (1) might also be expressed as

$$f \cdot PV < 0 \tag{3}$$

on isentropic levels (see, e.g., Knox & Harvey, 2005).

Knox and Harvey (2005) used relation (1) to construct their climatology of stratospheric II in UK Met Office analyses. Here we use the same criterion to investigate whether or not the pancake structures observed by RO and reproduced by ECMWF are indeed caused by II. Figures 3e and 3f show latitude-longitude cross sections of potential vorticity (PV) at $\theta = 1,000$ K (~34 ± 2-km altitude) and 2,000 K (~ 48 ± 3-km altitude), respectively. In the same figures, we marked regions with $\partial PV/\partial y < 0$ with black crosses. Regions with $f \cdot PV < 0$ are identified by negative values of PV (in red) since f is positive in the Northern Hemisphere (NH).

Indeed, the diagnostics reveal Rossby wave breaking which advects negative *PV* northward into the latitude-longitude region where the pancake structures are observed, that is, the region marked with a black rectangle. We note that this signature of Rossby wave breaking and related advection of negative *PV* is even more pronounced on 30 November (not shown), that is, just at the beginning of the event before the instability has started eliminating the region of anomalous vorticity.

In conclusion, the observed pancake structures have likely been caused by II at the equatorward edge of the PNJ in combination with Rossby wave breaking and the related northward advection of negative PV.

4.2. Climatology From ERA-Interim

Here we use the full ERA-Interim data set from 1979 to 2016 to investigate how exceptional or typical the II event of 3 December 2015 has been. For this purpose, computed daily values of mean zonal winds, minima of mean relative vorticities ξ, and mean total TP are displayed in Figures 4a–4c between 30- and 45-km altitude for 30–45°N and the three longitude ranges 90°W to 30°E, 30–150°E, and 150°E to 90°W.

Figure 4a reproduces the well-known annual cycle of the zonal wind with westerlies from mid-September through mid-May and easterlies during the rest of the year. During phases with eastward winds both u and ξ reveal a much larger variability than during the summer months. Figures 4b and 4c further show large negative minimum ξ values (and, hence, the tendency to satisfy criterion (1) along with large total TP during the same period. Note that the TP in Figure 4c do not contain significant contributions by GWs because of the large spatial area over which mean perturbations were derived (120° longitude by 15° latitude). Also, the short vertical cutoff wavelength of 15 km eliminates contributions from planetary waves and thermal tides to the perturbations because of their much longer λ_z (Pancheva & Mukhtarov, 2011). Thus, it is likely that most of the TP in Figure 4c are due to II. However, we cannot exclude contributions from other not yet identified large-scale instability processes which create TP at λ_z <15 km.

Finally, Figure 4d shows the cumulative probabilities of total TP ΔT_{total} for the period with large ΔT_{total} (mid-October to mid-April, in black) and for the rest of the year (in red). For completeness, Figure 4d shows cumulative probabilities for both NH (solid lines) and the Southern Hemisphere (SH, dashed lines). In agreement with the climatology of II occurrence by Knox and Harvey (2005) there also exists a SH midlatitude hot spot of II occurrence between 30°S and 45°S, which occurs 6 months later than in the NH. This comparison reveals very similar statistics in both hemispheres with a tendency for larger extreme amplitudes occurring in the NH. Please refer to the supporting information for more details on SH statistics.

Figure 4d clearly documents the much larger temperature variability in the period when II occurs as compared to the rest of the year: while 10% of the days during the period from mid-October to mid-April reveal ΔT_{total} of more than 5 K, the same is the case for only 0.01% during the rest of the year. Furthermore, we see that the large-amplitude event (with $\Delta T_{total} = 9.9$ K) of 3 December 2015, belonged to the 0.1% strongest events as derived from the ERA-Interim data set.

5. Summary and Conclusions

We presented RO observations of the spatial and temporal structure of large stratospheric TP which occurred during December 2015. The perturbations had vertical scales < 15 km and have previously been called pancakes due to their large-scale flat horizontal structure. The structures with peak-to-peak TP of ~10 K occurred both in the vicinity of the equator as well as at midlatitudes in the region 30–45°N in the longitude sector from 90°W to 45°E. The structures had a vertical wavelength of about 12 km, were 180° phase shifted between equatorial and midlatitudes at fixed altitude levels, and occurred in recurring *pulses* lasting up to 10 days. The observed patterns resemble previously described features associated with II.

Using high-resolution ECMWF operational analyses, we were able to show that the observed temperature structures were indeed generated by II caused by very large meridional shear of the zonal wind at the southern edge of an exceptionally strong PNJ in combination with Rossby wave breaking.

Finally, we analyzed the full ERA-Interim data set from 1979 to 2016 and found that large stratospheric TP do frequently occur in the period from October to April in the NH and from April to October in the SH. The temperature variability is much smaller outside this season: while 10% of the days during this period revealed $\Delta T_{\text{total}} > 5$ K, the same is the case for only 0.01% of the days outside the season. Furthermore, we found that the 3 December 2015 event observed by RO belonged to the 0.1% strongest TP (with $\Delta T_{\text{total}} = 9.9$ K) as derived from the ERA-Interim data set.

We conclude that II is an important source of stratospheric temperature variability at $\lambda_z < 15$ km from mid-October to mid-April at midlatitudes between 30°N and 45°N (and from mid-April to mid-October at 30–45°S). Hence, vertical analyses of temperature profiles used for constructing climatologies of GW activity from RO, other satellite limb-viewing observations, or ground-based lidar measurements likely also contain II and are thus high biased. This needs to be accounted for in constraining GW parameterizations for climate models. While it is well known that tropical Kelvin waves might contaminate such data in the tropics, the contribution from II documented here has largely been overlooked.

Acknowledgments
GPS RO data provision by EUMETSAT's ROM SAF is greatly appreciated. Access to the ECMWF data was possible through the special project *HALO Mission Support System*. RO data are available from www.romsaf.org. Details regarding access to ECMWF data can be found under www.ecmwf.int. Part of this research was conducted within the scope of the German research initiative *Role of the Middle Atmosphere in Climate (ROMIC)* under grant 01LG1206A by the German Ministry for Education and Research. Partial funding was also provided by the German Science Foundation (DFG) via the research unit MS-GWaves (GW-TP/DO 1020/9-1 and PACOG/RA 1400/6-1).

References

Alexander, M. J., Geller, M., McLandress, C., Polavarapu, S., Preusse, P., Sassi, F., et al. (2010). Recent developments in gravity-wave effects in climate models and the global distribution of gravity-wave momentum flux from observations and models. *Quarterly Journal of the Royal Meteorological Society*, *136*, 1103–1124. https://doi.org/10.1002/qj.637

Clark, P. D., & Haynes, P. H. (1996). Inertial instability on an asymmetric low-latitude flow. *Quarterly Journal of the Royal Meteorological Society*, *122*(529), 151–182. https://doi.org/10.1002/qj.49712252907

Dee, D. P., Uppala, S. M., Simmons, A. J., Berrisford, P., Poli, P., Kobayashi, S., et al. (2011). The era-interim reanalysis: Configuration and performance of the data assimilation system. *Quarterly Journal of the Royal Meteorological Society*, *137*(656), 553–597. https://doi.org/10.1002/qj.828

Dunkerton, T. J. (1981). On the inertial stability of the equatorial middle atmosphere. *Journal of the Atmospheric Sciences*, *38*(11), 2354–2364.

Ehard, B., Kaifler, B., Kaifler, N., & Rapp, M. (2015). Evaluation of methods for gravity wave extraction from middle-atmospheric lidar temperature measurements. *Atmospheric Measurement Techniques*, *8*(11), 4645–4655. https://doi.org/10.5194/amt-8-4645-2015

Ern, M., Trinh, Q. T., Preusse, P., Gille, J. C., Mlynczak, M. G., Russell III, J. M., & Riese, M. (2018). Gracile: A comprehensive climatology of atmospheric gravity wave parameters based on satellite limb soundings. *Earth System Science Data*, *10*(2), 857–892. https://doi.org/10.5194/essd-10-857-2018

Fritts, D. C., Yuan, L., Hitchman, M. H., Coy, L., Kudeki, E., & Woodman, R. F. (1992). Dynamics of the equatorial mesosphere observed using the Jicamarca MST radar during June and August 1987. *Journal of the Atmospheric Sciences*, *49*(24), 2353–2371.

Geller, M., Alexander, M. J., Love, P. T., Bacmeister, J., Ern, M., Hertzog, A., et al. (2013). A comparison between gravity wave momentum fluxes in observations and climate models. *Journal of Climate*, *26*, 6383–6405. https://doi.org/10.1175/JCLI-D-12-00545.1

Griffiths, S. D. (2003). Nonlinear vertical scale selection in equatorial inertial instability. *Journal of the Atmospheric Sciences*, *60*(7), 977–990.

Griffiths, S. D. (2008). The limiting form of inertial instability in geophysical flows. *Journal of Fluid Mechanics*, *605*, 115–143. https://doi.org/10.1017/S0022112008001407

Hayashi, H., Shiotani, M., & Gille, J. C. (1998). Vertically stacked temperature disturbances near the equatorial stratopause as seen in cryogenic limb array etalon spectrometer data. *Journal of Geophysical Research*, *103*(D16), 19,469–19,483. https://doi.org/10.1029/98JD01730

Hayashi, H., Shiotani, M., & Gille, J. C. (2002). Horizontal wind disturbances induced by inertial instability in the equatorial middle atmosphere as seen in rocketsonde observations. *Journal of Geophysical Research*, *107*(D14), 4228. https://doi.org/10.1029/2001JD000922

Hitchman, M. H., Leovy, C. B., Gille, J. C., & Bailey, P. L. (1987). Quasi-stationary zonally asymmetric circulations in the equatorial lower mesosphere. *Journal of the Atmospheric Sciences*, *44*(16), 2219–2236.

Knox, J. A., & Harvey, V. L. (2005). Global climatology of inertial instability and Rossby wave breaking in the stratosphere. *Journal of Geophysical Research*, *110*, D06108. https://doi.org/10.1029/2004JD005068

Kursinski, E. R., Hajj, G. A., Schofield, J. T., Linfield, R. P., & Hardy, K. R. (1997). Observing Earth's atmosphere with radio occultation measurements using the global positioning system. *Journal of Geophysical Research*, *102*(D19), 23,429–23,465.

Malardel, S., & Wedi, N. P. (2016). How does subgrid-scale parametrization influence nonlinear spectral energy fluxes in global NWP models? *Journal of Geophysical Research: Atmospheres*, *121*, 5395–5410. https://doi.org/10.1002/2015JD023970

Marquardt, C., & Healy, S. B. (2005). Measurement noise and stratospheric gravity wave characteristics obtained from GPS radio occultation. *Journal of the Meteorological Society of Japan*, *83*(3), 417–428.

Matthias, V., DÃuűrnbrack, A., & Stober, G. (2016). The extraordinarily strong and cold polar vortex in the early northern winter 2015/2016. *Geophysical Research Letters*, *43*, 12,287–12,294. https://doi.org/10.1002/2016GL071676

O'Sullivan, D. J., & Hitchman, M. H. (1992). Inertial instability and Rossby wave breaking in a numerical model. *Journal of the Atmospheric Sciences*, *49*(12), 991–1002.

Pancheva, D., & Mukhtarov, P. (2011). Atmospheric tides and planetary waves: Recent progress based on TIMED/SABER temperature measurements (2002–2007). In M. A. Abdu, D. Pancheva, & A. Bhattacharyya (Eds.), *Aeronomy of the Earth's atmosphere and ionosphere, IAGA Special Sopron Book Series* (Vol. 2, chap. 2, pp. 19–56). Dordrecht, Netherlands: Springer Science and Business Media B. V.

Preusse, P., Schaeler, B., Bacmeister, J. T., & Offermann, D. (1999). Evidence for gravity waves in CRISTA temperatures. *Advances in Space Research*, *24*(11), 1601–1604.

ROM SAF (2014). Product user manual: NRT and offline level 1 and level 2 products, EUMETSAT.

Randel, W. J., & Wu, F. (2005). Kelvin wave variability near the equatorial tropopause observed in GPS radio occultation measurements. *Journal of Geophysical Research*, *110*, D03102. https://doi.org/10.1029/2004JD005006

Rapp, M., Dörnbrack, A., & Kaifler, B. (2018). An intercomparison of stratospheric gravity wave potential energy densities from METOP GPS radio occultation measurements and ECMWF model data. *Atmospheric Measurement Techniques*, *11*(2), 1031–1048. https://doi.org/10.5194/amt-11-1031-2018

Rowe, S. M., & Hitchman, M. H. (2015). On the role of inertial instability in stratosphere-troposphere exchange near midlatitude cyclones. *Journal of the Atmospheric Sciences*, *72*(5), 2131–2151. https://doi.org/10.1175/JAS-D-14-0210.1

Rowe, S. M., & Hitchman, M. H. (2016). On the relationship between inertial instability, poleward momentum surges, and jet intensifications near midlatitude cyclones. *Journal of the Atmospheric Sciences*, *73*(6), 2299–2315. https://doi.org/10.1175/JAS-D-15-0183.1

Sato, K., & Dunkerton, T. J. (2002). Layered structure associated with low potential vorticity near the tropopause seen in high-resolution radiosondes over Japan. *Journal of the Atmospheric Sciences*, *59*(19), 2782–2800.

Schmidt, T., Alexander, P., & de la Torre, A. (2016). Stratospheric gravity wave momentum flux from radio occultations. *Journal of Geophysical Research: Atmospheres*, *121*, 4443–4467. https://doi.org/10.1002/2015JD024135

Smith, A. K., & Riese, M. (1999). Cryogenic Infrared Spectrometers and Telescopes for the Atmosphere (CRISTA) observations of tracer transport by inertially unstable circulations. *Journal of Geophysical Research*, *104*(D16), 19,171–19,182. https://doi.org/10.1029/1999JD900274

Thompson, C. F., Schultz, D. M., & Vaughan, G. (2018). A global climatology of tropospheric inertial instability. *Journal of the Atmospheric Sciences*, *75*(3), 805–825. https://doi.org/10.1175/JAS-D-17-0062.1

Tsuda, T., Nishida, M., Rocken, C., & Ware, R. (2000). A global morphology of gravity wave activity in the stratosphere revealed by the GPS occultation data (GPS/MET). *Journal of Geophysical Research*, *105*, 7257–7273.

Whiteway, J. A., & Carswell, A. I. (1995). Lidar observations of gravity wave activity in the upper stratosphere over Toronto. *Journal of Geophysical Research*, *100*(D7), 14,113–14,124. https://doi.org/10.1029/95JD00511